

# High-Order Harmonic Generations in Epsilon-Near-Zero Aluminum-Doped Zinc Oxide Nanopyramid Array

Jiaye Wu<sup>1</sup>, Ze Tao Xie<sup>1</sup>, H. Y. Fu<sup>2</sup>, Qian Li<sup>1,\*</sup>

<sup>1</sup> School of Electronic and Computer Engineering, Peking University, Shenzhen 518055, China

<sup>2</sup> Tsinghua-Berkeley Shenzhen Institute (TBSI), Tsinghua University, Shenzhen 518055, China

\* e-mail: liqian@pkusz.edu.cn

**Abstract**—We numerically demonstrate the high harmonic generations (HHGs) up to the seventh order in epsilon-near-zero (ENZ) aluminum-doped zinc oxide (AZO) nanopyramid array. Pumped by a 1-kHz repetition rate 50-mW 100-fs laser source at the telecommunication wavelength of 1550 nm, the conversion efficiencies of  $1.41 \times 10^{-5}$ ,  $3.64 \times 10^{-6}$ , and  $2.09 \times 10^{-7}$  are achieved for third-, fifth-, and seventh-harmonic generations, respectively, which are comparable with the experimental results of indium tin oxide and indium-doped cadmium oxide. The electric field distributions, localized resonances, and emission patterns at HHG wavelengths are also discussed. The results of this work can be potentially useful in designing novel multiwavelength light sources for optical communication and on-chip light circuits.

**Keywords**—epsilon-near-zero; high harmonic generations; metamaterial; metasurface; light sources; telecommunication; on-chip light circuits

## I. INTRODUCTION

Among the near-zero-index materials, epsilon-near-zero (ENZ) materials have been a heated topic in the regimes of nonlinear optics and nanophotonics. Near the cross-over wavelength where the real part of the complex permittivity slowly reduces to zero, a near-infinite phase velocity is shown and the electromagnetic (EM) wave can tunnel through the optical structure [1] with an unvaried phase [2], experience an enhanced electric field and slow-light trapping [3], as well as an enhanced nonlinearity in material [4].

Based on ENZ transparent conducting oxides' (TCOs) outstanding capability of producing large optical nonlinearity [5] and their high efficiency in frequency conversion [6], TCOs are found to exhibit complex pulse-matter interaction patterns under subwavelength setup [7]–[10] and exotic dispersion patterns [8], [11]. They can be used in electro- and all-optical switching and modulation [12]–[17]. TCOs also exhibit efficient second- [18], [19], third- [18], [20], [21], and high harmonic generations (HHG) [22] in their ENZ regions. However, the high-order harmonic generations in nanostructured aluminum-doped zinc oxide (AZO), a kind of ENZ TCOs, have not been analyzed. Nanostructures might allow performance enhancement or new optical phenomena to happen due to the edge (boundary) effects induced by their shapes and geometries.

In this work, we numerically demonstrate the HHGs (second- to the seventh-harmonic generations) in ENZ AZO

nanopyramid array using a 1-kHz repetition rate 50-mW 100-fs pump source at the telecommunication wavelength of 1550 nm. Spectral conversion efficiencies of  $1.41 \times 10^{-5}$ ,  $3.64 \times 10^{-6}$ , and  $2.09 \times 10^{-7}$  are achieved for third-, fifth-, and seventh-harmonic generations, which are comparable with the experimental results of indium tin oxide [21] (ITO, third-harmonic at  $\sim 3.3 \times 10^{-6}$ ) and indium-doped cadmium oxide [22] (ICO,  $\sim 10^{-5}$ ,  $\sim 10^{-8}$ , and  $\sim 10^{-10}$ ). The electric field distributions, localized resonances, and EM wave emission patterns at second- to seventh-order HHG wavelengths are also discussed. The proposed metasurface design can have great potential in designing novel multiwavelength light sources for future optical communication and on-chip integrated light circuits.

This paper is structured as follows. In Section II, the theory and models are introduced. In Section III, the results of high harmonic generations are analyzed. The conclusion of this work is drawn in Section IV.

## II. THEORY AND MODELS

The well-known and prestigious Drude model [23] has been proven to illustrate the complex permittivity of ENZ AZO accurately in its near-infrared ENZ region:

$$\begin{aligned}\varepsilon_R &= \varepsilon_b - \frac{\omega_p^2}{(\omega + i\gamma)\omega} \\ &= \varepsilon_r + i\varepsilon_i = \varepsilon_b - \frac{\omega_p^2}{(\omega^2 + \gamma^2)} + i \frac{\omega_p^2 \gamma}{(\omega^2 + \gamma^2)\omega},\end{aligned}\quad (1)$$

where  $\varepsilon_r$  and  $\varepsilon_i$  are the real and imaginary parts of the ENZ AZO.  $\varepsilon_b = 3.8$  is the high frequency permittivity,  $\omega$  is the angular frequency of the electromagnetic wave,  $\omega_p = 2.37 \times 10^{15}$  rad/s is the plasma frequency, and  $\gamma = 6.80 \times 10^{13}$  rad/s is the Drude relaxation rate [24]. The ENZ wavelength (cross-over point) where  $\varepsilon_r$  reaches zero locates exactly at the telecommunication wavelength of 1550 nm by tuning the free carrier concentration. Highly doped TCOs such as the ENZ AZO tend to have degraded second-order susceptibility ( $\chi^{(2)}$ ) [25] and a large third-order susceptibility ( $\chi^{(3)}$ ) [5], but experiments [26] have shown that  $\chi^{(2)}$  of AZO can exist near the surface, therefore,  $\chi^{(2)}$  and  $\chi^{(3)}$  of the ENZ AZO material are set to be  $9.93 \times 10^{-13}$  m/V and  $4.62 \times 10^{-22}$  m<sup>2</sup>/V<sup>2</sup> [26].

The schematic diagram of the designed ENZ AZO nanopyramid array and the geometry of its repeating unit cell are illustrated in Fig. 1. The length of the bottom edges of the pyramid are 200 nm, the height of the pyramid is 100 nm, and the spacing between every two pyramids is 200 nm, making the repeating nanostructure-substrate unit cell a 400 nm × 400 nm square block. The substrate is pure silica glass, which is a commonly-used substrate to grow AZO.

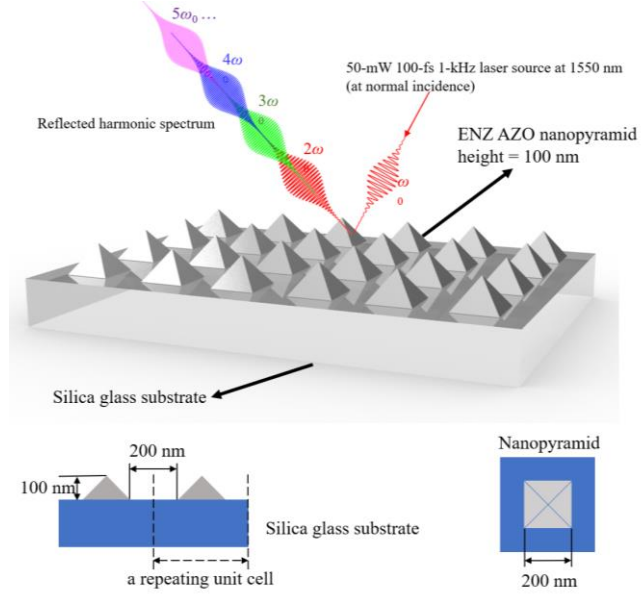


Figure 1. <sup>a</sup> The schematic diagram of the ENZ AZO nanopyramid array. The top half of the figure shows the arrangement of the array, and the bottom half shows the geometry of the ENZ AZO nanopyramid-substrate unit cell. The 100-nm-high 200 nm × 200 nm pyramids are fabricated on silica glass substrate, with a 200-nm spacing between each two nanopyramids.

The metasurface of the ENZ AZO nanopyramid array can be fabricated using various techniques like magnetron sputtering, and etched by either ultraviolet excimer laser or chemicals. These processes are compatible with modern CMOS technologies. The AZO nanopyramid array design can provide a wide range of incident and emission angles, allowing energy localization and radiation at surfaces and edges.

To simulate the interaction of the EM wave in the ENZ AZO nanopyramid array, the nonlinear Maxwell's equations are considered [27] to include the effects of second harmonic generation and sum frequency generation of  $\chi^{(2)}$  and the effects of Kerr nonlinearity and third harmonic generation of  $\chi^{(3)}$ . The detailed implementation is:

$$\begin{aligned} \nabla \times \mathbf{H} &= \frac{\partial \mathbf{D}}{\partial t}, \nabla \times \mathbf{E} = -\frac{\partial \mathbf{B}}{\partial t}, \\ \mathbf{D} &= \varepsilon_0 \mathbf{E} + \mathbf{P}_L + \mathbf{P}_{NL}, \mathbf{B} = \mu_0 \mathbf{H} \\ \mathbf{P}_L &= \varepsilon_0 \chi^{(1)} \cdot \mathbf{E}, \\ \mathbf{P}_{NL} &= \varepsilon_0 \left( \chi^{(2)} : \mathbf{E}\mathbf{E} + \chi^{(3)} : \mathbf{E}\mathbf{E}\mathbf{E} \right). \end{aligned} \quad (2)$$

Here, the vacuum permittivity  $\varepsilon_0 = 8.85 \times 10^{-12}$  F/m and the vacuum permeability  $\mu_0 = 4\pi \times 10^{-7}$  N/A<sup>2</sup>.  $\mathbf{E}$  and  $\mathbf{H}$  are electric and magnetic fields,  $\mathbf{D}$  and  $\mathbf{B}$  are electric and magnetic inductions.  $\mathbf{P}_L$  and  $\mathbf{P}_{NL}$  are the linear and nonlinear electric polarizations, and they are closely related to the first-, second- and third-order susceptibilities  $\chi^{(1)}$ ,  $\chi^{(2)}$ , and  $\chi^{(3)}$  as shown in Eq. (2). It is worth noting that,  $\chi^{(1)} = \varepsilon_R - 1$ , which means that when the first two terms of  $\mathbf{D}$  are added, they become  $\varepsilon_0 \varepsilon_R \mathbf{E}$ . Therefore, the permittivity curves obtained by Eq. (1) is sufficient and accurate to describe the effects of  $\chi^{(1)}$ , and the single  $\chi^{(1)}$  value at 1550 nm should be avoided in the simulation. On the other hand, it is tedious and nearly impossible to manually solve Eq. (2) for a very wide range of wavelengths, and in the simulations of this work, Eq. (2) is numerically solved by the commercially available software by Lumerical using finite-difference time-domain (FDTD) method.

### III. HIGH-ORDER HARMONIC GENERATIONS

To excite HHGs in ENZ AZO nanopyramid array, a 1-kHz repetition rate 50-mW 100-fs 1-kHz laser pump source at telecommunication wavelength of 1550 nm is used. Assuming a focused laser spot radius of 5  $\mu\text{m}$ , an average intensity of  $6.37 \times 10^4$  W/cm<sup>2</sup> is acquired, which corresponds to a peak intensity of  $6.37 \times 10^{14}$  W/cm<sup>2</sup> and a peak electric field amplitude in vacuum of  $6.93 \times 10^{10}$  V/m. This intensive electric field enables HHGs to emerge from the spectrum, as well as drives the frequency conversion between each spectral component. The waveform of the pulse is chirp-free Gaussian, and the pulse is injected onto the nanostructures at normal incidence. These incident pulses are *p*-polarized and the polarization direction is parallel to the *x* axis in Fig. 3. The data are collected from the reflection spectrum above the sample. The numerical results show that the designed ENZ AZO nanopyramid array can produce second- to seventh-harmonic generations, as shown in Fig. 2(a). Due to the fact that, the higher the HHG order is, the closer the wavelengths are to its adjacent order. Therefore, it is hard to see higher order HHGs in Fig. 2(a), and we expanded it as the integer multiples of the base frequency in Fig. 2(b). From Fig. 2(b), one can clearly see that the HHGs up to the seventh order. In Fig. 2, the input spectra are shown in red lines, while the output reflected spectra are shown in blue lines.

In Fig. 2(a), the spectral locations of the second-, third-, fourth-, fifth-, sixth-, and seventh-harmonic generations are, 775 nm, 516.7 nm, 387.5 nm, 310 nm, 258.3 nm, and 221.43 nm, respectively. Their corresponding relative intensity values are,  $1.15 \times 10^{-7}$ ,  $1.41 \times 10^{-5}$ ,  $2.96 \times 10^{-8}$ ,  $3.64 \times 10^{-6}$ ,  $2.05 \times 10^{-9}$ , and  $2.09 \times 10^{-7}$ , respectively. In order to roughly estimate the conversion efficiency of the HHGs, one can calculate the ratio between the intensity of the generated harmonic wave and the intensity of the input light source, and this is called a spectral conversion efficiency (SCE). Under this definition, the SCEs of the third-, fifth-, and seventh-harmonic generation are  $1.41 \times 10^{-5}$ ,  $3.64 \times 10^{-6}$ , and  $2.09 \times 10^{-7}$ . In theory, these values are comparable with the experimental record of ENZ ITO [21] (third-harmonic at  $\sim 3.3 \times 10^{-6}$ ) and ENZ ICO [22] ( $\sim 10^{-5}$ ,  $\sim 10^{-8}$ , and  $\sim 10^{-10}$ ).

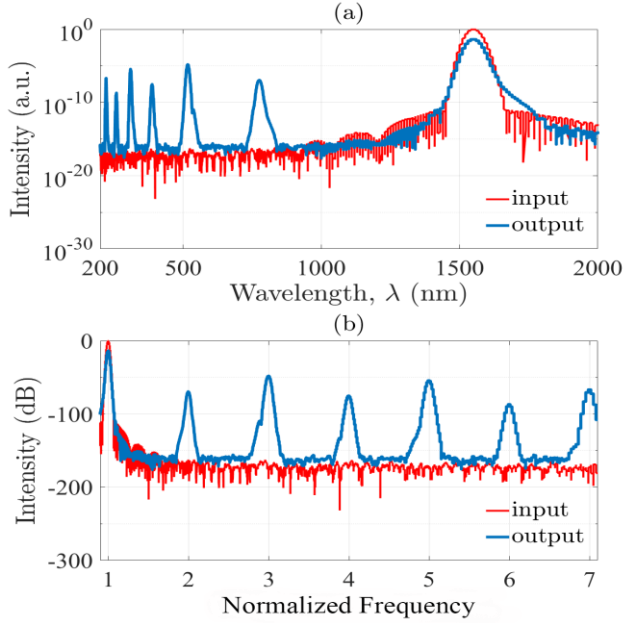


Figure 2. " (a) The normalized spectrum of the second-, third-, fourth-, fifth-, sixth-, and seventh-harmonic generations and (b) the normalized frequency view of the generated HHGs in multiples of the base telecom frequency. The red lines denote the input spectra and the blue lines are the output reflected spectra.

ENZ TCO material often suffers significant loss, and to demonstrate this, the temporal shapes between the input pulse and the output spectrum is shown in Fig. 3. In Fig. 3, the input temporal shape of the pulse is shown in the oscillating red line, while the temporal shape of the output spectrum is shown in blue line.

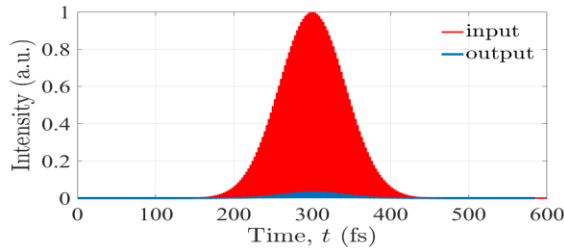


Figure 3. " The temporal shapes of the input Gaussian pulse and the output HHG spectrum. The input pulse's temporal shape is shown in the red line, while that of the output spectrum is shown in blue line.

In Fig. 3, the output temporal peak intensity is only 3.63% of the input pulse, indicating a large intrinsic loss inherent in the ENZ AZO material. The intrinsic loss limits the application of ENZ TCOs in large-scale devices, and they are only suitable for nanophotonic devices.

The ENZ AZO nanopyramid array can exhibit exclusive electric field distributions, localized resonances, and EM wave emission patterns at HHG wavelengths. In order to investigate this, the diagrams of the normalized electric field distributions of a single unit cell of the designed ENZ AZO nanopyramid array at the corresponding HHG wavelengths

are shown in Fig. 4, and the outlines and boundaries of the nanopyramid is represented as white dashed lines.

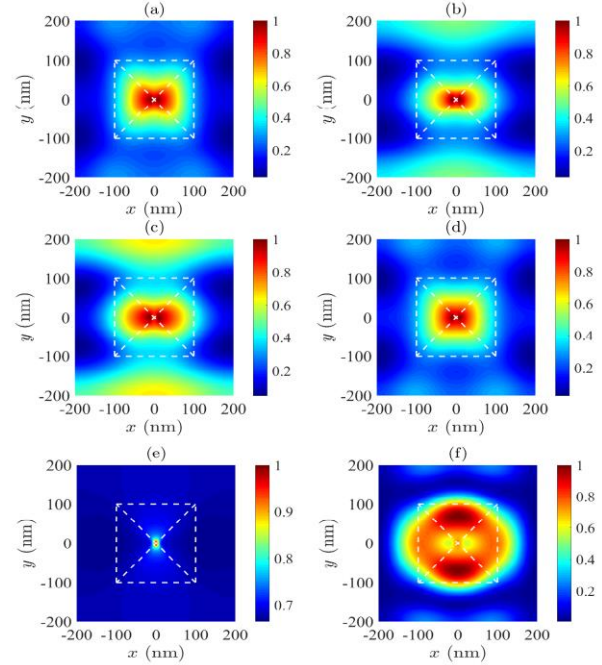


Figure 4. " The normalized electric field intensity distributions, localized resonances, and emission patterns at (a) second-harmonic wavelength of 775 nm, (b) third-harmonic wavelength of 516.7 nm, (c) fourth-harmonic wavelength of 387.5 nm, (d) fifth-harmonic wavelength of 310 nm, (e) sixth-harmonic wavelength of 258.3 nm, and (f) seventh-harmonic wavelength of 221.43 nm of a single unit cell of the designed ENZ AZO nanopyramid array. The white dashed lines denote the outlines and boundaries of the nanopyramid structure.

In Fig. 4(a), for the second-harmonic wavelength, the electric field is localized at the tip and the body of the pyramid. The energy is confined in the boundaries of the nanostructure. With the area around the tip being the strongest, the nanoantenna effect of the array might allow EM wave emission at the center of the structure. From Fig. 4(b), the typical periodic patterns from the unit cells on the adjacent top and bottom can be observed. The EM energy is less confined compared with Fig. 4(a) and the pattern is quite different from the latter. Figure 4(c) shows a similar pattern to Fig. 4(b), but the field is again, less confined than Fig. 4(b). The EM field outside the nanostructure tends to "connect" with the field inside, and due to the relatively weaker confinement, radiation mode is possible and likely for this wavelength. Figure 4(d) resembles Fig. 4(a) with a confined field but slightly different details. These mean that the HHG EM wave emission (radiation) for the second- and fifth-harmonic generations are probably weaker than the third- and the fourth-harmonic. Figure 4(e) shows localized energy only at the tip of the pyramid, and Fig. 4(f) exhibits a non-confined field distribution. In Fig. 4(f), the field extends far beyond the boundaries of the nanopyramid, which might indicate a strong radiation mode.

The second- to the seventh-harmonic wavelengths are all located to the left of the ENZ wavelength and inside the “dielectric” zone where the material behaves like a normal dielectric material. However, the ENZ effect still has a role to play, and the efficient frequency conversion at ENZ wavelength ensures the high efficiencies in harmonic generations. On the other hand, the field patterns at harmonic wavelengths are due to the boundary effects of the nanostructures, allowing localized resonances and harmonic EM wave emission to happen. The presented patterns of the electric fields in this work might be helpful in the future optimization of the HHG-wave-emitting nanoantenna arrays, creating novel forms of multiwavelength integrated on-chip light sources.

#### IV. CONCLUSION

We numerically demonstrate the HHGs up to the seventh order in an ENZ AZO nanopillar array. With proper pumping, at the ENZ wavelength of 1550 nm, the nanopillar array is capable of generating HHG waves at high efficiency. High SCEs of  $1.41 \times 10^{-5}$ ,  $3.64 \times 10^{-6}$ , and  $2.09 \times 10^{-7}$  are obtained for the third-, fifth-, and seventh-harmonic generations. These values are comparable with the experimental record of ENZ ITO (third-harmonic at  $\sim 3.3 \times 10^{-6}$ ) and ENZ ICO ( $\sim 10^{-5}$ ,  $\sim 10^{-8}$ , and  $\sim 10^{-10}$ ). The electric field distributions, localized resonances, and EM emission patterns at second- to seventh-order HHG wavelengths are also discussed, and the distinctive resonance patterns at different HHGs reveals the potential in designing novel HHG-wave-emitting nanoantenna arrays. The results of this work can be potentially useful in designing novel light sources for telecommunication and on-chip light circuits.

#### ACKNOWLEDGMENT

This work is supported by the National Natural Science Foundation of China (Grant No. 61675008), Shenzhen Science and Technology Innovation Commission (Grant No. GJHZ2018411185015272, JCYJ20180507183815699), and Youth Science and Technology Innovation Talent of Guangdong Province (Grant No. 2019TQ05X227).

#### REFERENCES

- [1] M. Silveirinha and N. Engheta, “Tunneling of Electromagnetic Energy through Subwavelength Channels and Bends using  $\epsilon$ -Near-Zero Materials,” *Phys. Rev. Lett.*, vol. 97, no. 15, p. 157403, Oct. 2006, doi: 10.1103/PhysRevLett.97.157403.
- [2] S. Enoch, G. Tayeb, P. Sabouroux, N. Guérin, and P. Vincent, “A Metamaterial for Directive Emission,” *Phys. Rev. Lett.*, vol. 89, no. 21, p. 213902, Nov. 2002, doi: 10.1103/PhysRevLett.89.213902.
- [3] A. Ciattoni, A. Marini, C. Rizza, M. Scalora, and F. Biancalana, “Polariton excitation in epsilon-near-zero slabs: Transient trapping of slow light,” *Phys. Rev. A*, vol. 87, no. 5, p. 053853, May 2013, doi: 10.1103/PhysRevA.87.053853.
- [4] A. Ciattoni, C. Rizza, A. Marini, A. Di Falco, D. Faccio, and M. Scalora, “Enhanced nonlinear effects in pulse propagation through epsilon-near-zero media,” *Laser Photon. Rev.*, vol. 10, no. 3, pp. 517–525, May 2016, doi: 10.1002/lpor.201500326.
- [5] M. Z. Alam, I. De Leon, and R. W. Boyd, “Large optical nonlinearity of indium tin oxide in its epsilon-near-zero region,” *Science*, vol. 352, no. 6287, pp. 795–797, May 2016, doi: 10.1126/science.aae0330.
- [6] J. B. Khurgin *et al.*, “Adiabatic frequency shifting in epsilon-near-zero materials: the role of group velocity,” *Optica*, vol. 7, no. 3, p. 226, Mar. 2020, doi: 10.1364/OPTICA.374788.
- [7] J. Wu, B. A. Malomed, H. Y. Fu, and Q. Li, “Self-interaction of ultrashort pulses in an epsilon-near-zero nonlinear material at the telecom wavelength,” *Opt. Express*, vol. 27, no. 26, pp. 37298–37306, Dec. 2019, doi: 10.1364/OE.27.037298.
- [8] J. Wu, Z. T. Xie, Y. Sha, H. Y. Fu, and Q. Li, “Comparative study on epsilon-near-zero transparent conducting oxides: High-order chromatic dispersions and modeling of ultrashort pulse interactions,” *Phys. Rev. A*, vol. 102, p. 053503, 2020, doi: 10.1103/PhysRevA.102.053503.
- [9] J. Wu and Q. Li, “Propagation of Ultrashort Pulses in Indium Tin Oxide Epsilon-Near-Zero Subwavelength Metamaterial at 2  $\mu\text{m}$ ,” in *Frontiers in Optics + Laser Science APS/DLS*, 2019, p. JTU3A.28, doi: 10.1364/FIO.2019.JTU3A.28.
- [10] J. Wu and Q. Li, “Ultrashort Pulses in Indium Tin Oxide Thin Film at its Epsilon-Near-Zero Wavelength,” in *Asia Communications and Photonics Conference*, 2019, p. M4A.300.
- [11] J. Wu, Z. T. Xie, Y. Sha, H. Y. Fu, and Q. Li, “Large and Complex Chromatic Dispersion Profile in Epsilon-Near-Zero Aluminum-Doped Zinc Oxide,” in *Frontiers in Optics + Laser Science APS/DLS*, 2020, p. JTU1A.34.
- [12] N. Kinsey, C. DeVault, J. Kim, M. Ferrera, V. M. Shalae, and A. Boltasseva, “Epsilon-near-zero Al-doped ZnO for ultrafast switching at telecom wavelengths,” *Optica*, vol. 2, no. 7, p. 616, Jul. 2015, doi: 10.1364/OPTICA.2.000616.
- [13] Q. Guo *et al.*, “A Solution-Processed Ultrafast Optical Switch Based on a Nanostructured Epsilon-Near-Zero Medium,” *Adv. Mater.*, vol. 29, no. 27, p. 1700754, Jul. 2017, doi: 10.1002/adma.201700754.
- [14] Z. T. Xie, J. Wu, H. Y. Fu, and Q. Li, “Tunable Electro- and All-Optical Switch Based on Epsilon-Near-Zero Metasurface,” *IEEE Photonics J.*, vol. 12, no. 4, pp. 1–10, Aug. 2020, doi: 10.1109/JPHOT.2020.3010284.
- [15] M. G. Wood *et al.*, “Gigahertz speed operation of epsilon-near-zero silicon photonic modulators,” *Optica*, vol. 5, no. 3, p. 233, Mar. 2018, doi: 10.1364/OPTICA.5.000233.
- [16] Z. T. Xie, J. Wu, H. Y. Fu, and Q. Li, “Tunable Electro-Optical Metasurface Based on an Ultra-Strong Coupling Epsilon-Near-Zero System,” in *Frontiers in Optics + Laser Science APS/DLS*, 2020, p. JTU1A.41.
- [17] Y. Sha, J. Wu, Z. T. Xie, and Q. Li, “Optimization of Slot Waveguide Modulator Based on Epsilon-Near-Zero Effect,” in *Frontiers in Optics + Laser Science APS/DLS*, 2020, p. JM6A.24.
- [18] L. Rodríguez-Suné *et al.*, “Study of second and third harmonic generation from an indium tin oxide nanolayer: Influence of nonlocal effects and hot electrons,” *APL Photonics*, vol. 5, no. 1, p. 010801, Jan. 2020, doi: 10.1063/1.5129627.
- [19] A. Capretti, Y. Wang, N. Engheta, and L. Dal Negro, “Comparative Study of Second-Harmonic Generation from Epsilon-Near-Zero Indium Tin Oxide and Titanium Nitride Nanolayers Excited in the Near-Infrared Spectral Range,” *ACS Photonics*, vol. 2, no. 11, pp. 1584–1591, Nov. 2015, doi: 10.1021/acsphotonics.5b00355.
- [20] A. Capretti, Y. Wang, N. Engheta, and L. Dal Negro, “Enhanced third-harmonic generation in Si-compatible epsilon-near-zero indium tin oxide nanolayers,” *Opt. Lett.*, vol. 40, no. 7, p. 1500, Apr. 2015, doi: 10.1364/OL.40.001500.
- [21] T. S. Luk *et al.*, “Enhanced third harmonic generation from the epsilon-near-zero modes of ultrathin films,” *Appl. Phys. Lett.*, vol. 106, no. 15, p. 151103, Apr. 2015, doi: 10.1063/1.4917457.
- [22] Y. Yang *et al.*, “High-harmonic generation from an epsilon-near-zero material,” *Nat. Phys.*, vol. 15, no. 10, pp. 1022–1026, Oct. 2019, doi: 10.1038/s41567-019-0584-7.
- [23] P. Drude, “Zur Elektronentheorie der Metalle,” *Ann. Phys.*, vol. 306, no. 3, pp. 566–613, 1900, doi: 10.1002/andp.19003060312.

- [24] G. V. Naik, V. M. Shalaev, and A. Boltasseva, “Alternative Plasmonic Materials: Beyond Gold and Silver,” *Adv. Mater.*, vol. 25, no. 24, pp. 3264–3294, Jun. 2013, doi: 10.1002/adma.201205076.
- [25] J. Kim *et al.*, “Optical Properties of Gallium-Doped Zinc Oxide—A Low-Loss Plasmonic Material: First-Principles Theory and Experiment,” *Phys. Rev. X*, vol. 3, no. 4, p. 041037, Dec. 2013, doi: 10.1103/PhysRevX.3.041037.
- [26] W. Tian *et al.*, “Highly Efficient Super-Continuum Generation on an Epsilon-Near-Zero Surface,” *ACS Omega*, vol. 5, no. 5, pp. 2458–2464, Feb. 2020, doi: 10.1021/acsomega.9b04026.
- [27] G. P. Agrawal, *Nonlinear Fiber Optics*, 5th ed. Oxford, United Kingdom: Academic Press, 2013.